

Three-dimensional Motor Neuron Morphology Estimation in the *Drosophila* Ventral Nerve Cord

Gavriil Tsechpenakis*, *Member IEEE*, Prateep Mukherjee, Michael D. Kim, and Akira Chiba

Abstract—Type-specific dendritic arborization patterns dictate synaptic connectivity and are fundamental determinants of neuronal function. We exploit the morphological stereotypy and relative simplicity of the *Drosophila* nervous system to model the diverse neuronal morphologies of individual motor neurons (MNs) and understand underlying principles of synaptic connectivity in a motor circuit. Our computational approach aims at the reconstruction of the neuron morphology, namely the robust segmentation of the neuron volumes from their surroundings with the simultaneous partitioning into their compartments, namely the soma, axon and dendrites. We use the idea of co-segmentation, where every image along the z-axis (depth) is segmented using information from ‘neighboring’ depths. We use 3D Haar-like features to model appearance. Because soma and axon are determined by their distinctive shapes, we define an implicit shape representation of the 2D segmentation sets to drive co-segmentation and achieve the desired partitioning. We validate our method using image stacks depicting single neurons labeled with green fluorescent protein (GFP) and serially imaged with laser scanning confocal microscopy.

Index Terms—neuron morphology, neuron compartment-based labeling, co-segmentation, 3d Haar features, *Drosophila*

I. INTRODUCTION

Normal locomotive behavior is fundamentally determined by precise patterns of motor neuron (MN) connectivity that are dictated by the selective connection of motor axons with muscle targets as well as specific dendritic input from presynaptic neurons. In the vertebrate spinal cord, MNs are organized into columns based on axonal projection patterns and within these columns, groups of MNs that target individual muscles are clustered into MN pools [19], [20]. Different MN pools elaborate distinct dendritic arborization patterns and respond to sensory stimulation with different latencies, demonstrating that the selectivity of synaptic input is directly influenced by the differential patterning of MN dendrites in the spinal cord [36].

Therefore, determining how different MN subtypes pattern and organize their dendrites in 3D space will be a crucial

G. Tsechpenakis is with the Computer and Information Science Department, Indiana University-Purdue University Indianapolis, USA. Email: gavriil@cs.iupui.edu

P. Mukherjee is with the Computer and Information Science Department, Indiana University-Purdue University Indianapolis, USA. Email: mukherjeeprateep@gmail.com

M.D. Kim is with the Molecular and Cellular Pharmacology Department, University of Miami Miller School of Medicine, USA. Email: mkim2@med.miami.edu

A. Chiba is with the Biology Department, University of Miami, USA. Email: akira.chiba@me.com

This work is supported in part by NSF/DBI [#1062405]: ‘ABI Innovation: Modeling the *Drosophila* Brain with Single-neuron Resolution using Computer Vision Methods’, awarded to G. Tsechpenakis, NIH/NINDS [5RC2NS069488-02]: ‘In Situ Protein-Protein Interaction Networks of Neurons (isPIN)’, awarded to A. Chiba, and NIH/NINDS [NS072588]: ‘Genetic Mechanisms of Motor Neuron Degeneration’, awarded to M.D. Kim.

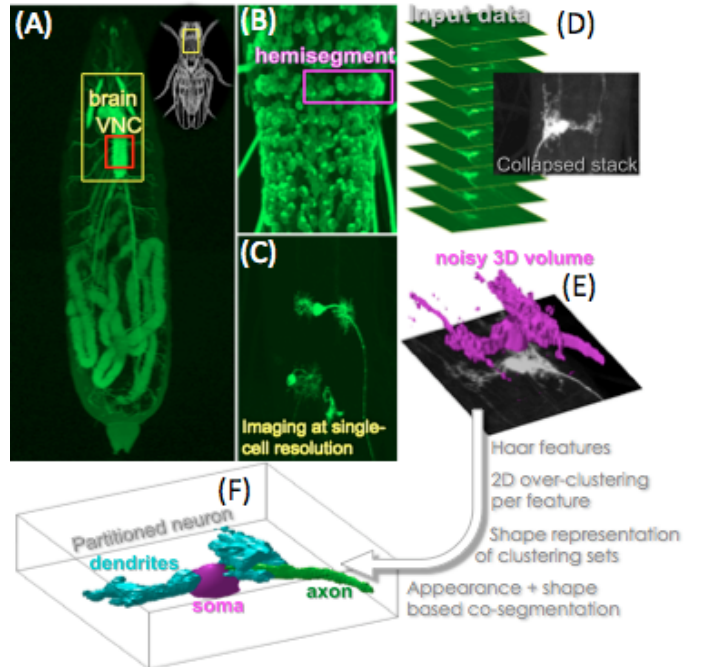


Fig. 1. (A) The whole larva with expressed GFP [23] (all motor neurons are shown). The panel also shows the Central Nervous System (CNS), i.e., brain and Ventral Nerve Cord (VNC), in relation to the whole animal. (B) Magnification of the VNC. (C) Using a genetic technique known as MARCM, we generate single MN clones which we analyze. (D) An image stack produced with laser scanning confocal microscopy; the 2D image results from intensity summation over depth. (E) Noisy neuron volume from the data in (D). Using a set of H Haar features we: (i) produce H over-segmentation sets for each image in the stack, one for each feature; (ii) define implicit shape representations to describe the topology of a segmentation set; (iii) integrate shape information of all segmentation outcomes, over all images (depths) and Haar features, to segment the neuron volume from its surroundings and partition it into its morphological compartments (soma, axon, dendrites). (F) The final outcome of our approach.

step toward understanding how motor circuits are assembled to control locomotion.

Our goal is to understand how connectivity patterns are formed within a normal motor circuit and determine whether a ‘connectivity map’ can be deduced by estimations of neuronal morphology. Also, developing a 3D model standard for different MN subtypes will allow for unbiased determinations of differences between neuronal morphologies in a wild-type and mutant brain. This will greatly facilitate our investigation into how different MN subtypes pattern their dendritic arbor to establish synaptic connectivity, which remains an understudied yet important aspect of motor circuit formation. Lastly, understanding the normal process of MN development will ultimately be important in devising strategies to repair or

restore MN connectivity after spinal cord injury or disease.

A. *Drosophila larvae as a model*

The *Drosophila* embryonic central nervous system (CNS) comprises the developing brain and ventral nerve cord (VNC) (Fig. 1A). The VNC, which can be considered functionally orthologous to the mammalian spinal cord, is segmentally reiterated and bilaterally symmetrical with respect to the ventral midline. There are approximately 400 neurons, including an estimated 38 MNs, within each hemisegment (or half-segment) of the VNC (Fig. 1B). Abdominal hemisegments in the embryo comprise 30 stereotyped body wall muscles, each of which is innervated by one or more of the 38 MNs. The muscle innervation pattern of individual MNs is further highly stereotyped making embryonic MNs uniquely identifiable [18]. During larval development, dendrites of these abdominal MNs undergo considerable growth and dendritic branching is dramatically increased, likely reflecting extensive changes in synaptic connectivity that are required for more complex larval behaviors such as the peristaltic movements required for normal locomotion. Whether larval MNs project their dendrites to stereotyped regions of the VNC to create a connectivity map is unclear.

B. *Imaging at single-cell resolution*

Previous efforts to visualize morphology of single MNs have relied on dye-backfilling methods such as DiI. DiI is a lipophilic dye that is taken up by the axon and diffuses along the cell membrane to reveal neuronal morphology. However, this technique is limited in that neurons can only be labeled one at a time and dye-labeled neurons are more prone to photobleaching and phototoxicity. Furthermore, dye-labeling methods are not compatible with long-term sample preservation, limiting the use of secondary markers.

To overcome these limitations, we use mosaic analysis with a repressible cell marker (MARCM) [21], a genetic technique that allows us to label and image individual MNs (Fig. 1C). The use of fluorescent proteins allows for high-resolution *in vivo* imaging with minimal photobleaching, reduced phototoxicity and enhanced labeling of the neuronal membrane. Although labeled MNs generated by MARCM can be imaged live in the intact animal, muscle contraction by larva hinders the acquisition of confocal images through consecutive z positions. The brain and VNC are therefore exposed by dissection and the tissue is fixed with formaldehyde before immunostaining with antibodies directed against mCD8 and a secondary marker, Fasciclin II (FasII). FasII labels axon fascicles that divide the VNC into distinct territories and provides a frame of reference in which to map the relative positions of the MN soma and dendrites [17]. The entire morphology of single MNs is then imaged with laser scanning confocal microscopy that produces the image stacks to be analyzed (Fig. 2). Here we use only the green channel for the estimation of the neuron morphology (Fig. 1D-F), while the morphology-based MN classification requires datasets from both channels and is beyond the scopes of this paper.

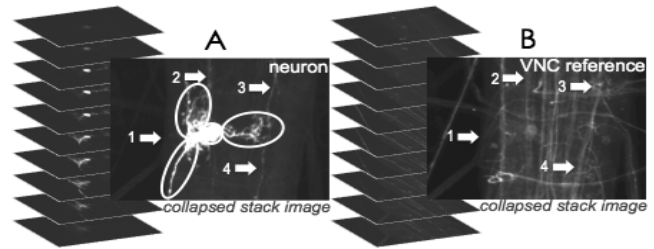


Fig. 2. Datasets for classifying individual neurons: the image stacks, one for each channel; A: neuron images; B: CNS reference images. The circled areas in A indicate the neuron partitions of our interest (soma, axon, dendrites), while the numbered arrows show some features from VNC that inevitably exist in the mCD8-stained stack and we consider as noise.

C. *Partial neuron structure estimation in fine scales*

In the last decade there has been an increasing interest in the problem of segmenting tubular and tree-like structures such as the neuron dendrites. For example, Zhou et al. [38] use a level set-based approach to segment precisely dendrites from 2-photon microscopy images. Peng et al. [25] reconstruct neurites (axons and dendrites) with fuzzy boundaries using a region-based deformable model initialized by detecting neurite regions and connecting them in a shortest-path manner. In the work of [29], the tubular-like structures are segmented with shape-constrained geodesic active contours, after branching points are manually annotated in dendrites imaged with confocal microscopy, while in [1] a method for automated branching points detection is presented. In [33], the tree structure of the dendrites is estimated from multi-photon microscopic images, using skeletonization and splines. Dima et al. [6] use wavelets to trace the branches boundaries, while Uehara et al. [32] use confocal and 2-photon microscopy images to show a shape-driven approach where the dendrite branches are approximated with cylinders that serve as topology constraints for a wave propagation method. In the work of [22], dendrite structures are estimated by detecting their skeletons and then applying intensity-based fuzzy c-means clustering, while in [37] the detected skeletons are used in a graph-theoretic approach to provide fine tracing of the dendritic branches. In [9] a probabilistic method is proposed, where both local (in a single image) and global (over the entire image stack) constraints are considered in a K-Minimum Spanning Tree approach. In the recent work of Kaynig et al. [15] neuron boundaries are estimated from electron microscopy data with an energy minimization using graph cuts. Finally, it is worth noting the existence of software packages, such as NeuroLucida¹, used in [30] for tracing dendritic structures and calculating their morphology statistics, and NeuronStudio².

D. *Global neuron structure estimation*

According to the study in [16], the morphological features that uniquely describe individual MN subtypes are: relative position between the soma and the CNS center; relative position between the axon and the CNS center; direction and extent of the axon; position of the dendrites along the axon; relative positions of the dendrites and the soma; extent of

¹MBF Bioscience: <http://www.mbfbioscience.com/neuroLucida>

²Computational Neurobiology and Imaging Center, Mount Sinai School of Medicine, NY: <http://research.mssm.edu/cnic/tools-ns.html>

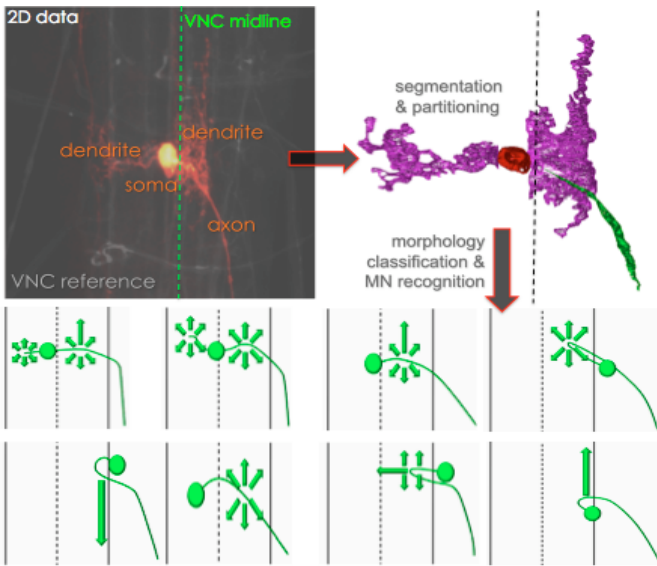


Fig. 3. Scope of the global neuron morphology estimation. From the neuron volume (collapsed stack image shown), our goal is the 3D segmentation/partitioning of the morphological compartments, for the estimation of their relative positions with respect to each other and the VNC reference (midline). This representation can yield the MN classification into distinct morphologies, shown with the (2D ground-truth) sketches and described in [16]: the arrows show the dendrites positions and extends, the disks illustrate the somata, the curved lines show the axons, while the dotted lines represent the VNC midline. The eight sketches correspond to different motor neurons from four main nerve branches (ISN, ISNb, ISNd, SNa): **top row, left to right:** [ISN: MN1-Ib], [ISN: MN9-Ib, MN10-Ib], [ISN: MN2-Ib], [ISN: MN3-Ib, MN4-Ib]; **bottom row, left to right:** [ISN: MN11-Ib, MN18-Ib, MN19-Ib, MN20-Ib], [ISNb: MN6/7-Ib, MN12-Ib, MN13-Ib, MN14-Ib, MN30-Ib, MNISNb/d-Is, MNISNb/d-II; ISNd: MN15/16/17-Ib], [ISNb: MN15/16-Ib], [SNa: MN21/22-Ib, MN22/23-Ib, MN23/24-Ib]. For further details we refer the reader to the study in [16].

the dendrites. To calculate these features, and apart from the segmentation of the neuron volume from its surroundings, we need to estimate the positions and shapes of the individual compartments, namely the soma, axon and dendrites. That is, we need to partition the neuron volume into these three morphologically distinct sub-volumes (Fig. 3).

From the above it is clear that here our goal is not to estimate the neurites structure in fine scales, but to provide a computationally comprehensive description for the entire structure of larval motor neurons, with simultaneous segmentation and labeling of the individual morphological compartments. This is the novelty of the present work. We base our study on the detailed descriptions of larval motor neurons in *Drosophila* found in the literature, namely the works of [16], [12], [28].

In summary, there are two major differences between our work and the literature above: (i) we are not interested in the precise segmentation of the dendritic structures, i.e., tracing the branches and detecting bifurcations, since this yields only a fraction of the desired morphology information; (ii) computationally, our task is the segmentation and compartment labeling, while existing image analysis techniques aim only at the segmentation of a part of the neuron, i.e., dendrites only or neurites.

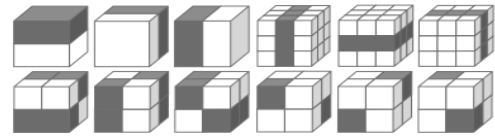


Fig. 4. Examples of the Haar masks in the 3D domain: {gray = -1, white = +1}.

II. NEURON MORPHOLOGY ESTIMATION

From Figs. 1, 2 it becomes apparent that while intensity determines the neuron volume, shape is what describes the compartment label: soma is an ellipsoid, axon is an elongated structure, while dendrites have arbitrary shapes.

The high variability in morphology, even for MNs of the same subtype, does not allow for partitioning using shape-constrained models, e.g., Active Shape Models [4]. Other model-based methods, such as the multi-compartment level set proposed in [7], can be best described as top-down, since they assume *a priori* known topology of the individual compartments during the initialization. Appearance-based methods, such as multi-label graph cuts [10], also consider approximations for the compartment relative topology, and ignore shape information. In our problem, the relative topology is unknown and it is the objective, in the bottom-up framework we describe below.

Our approach is based on the principle of co-segmentation [26], [14]. It exploits the idea of sharing information about the targets appearance and shape throughout the input set, instead of using prior knowledge, e.g. training samples in a supervised learning framework.

Co-segmentation principle was introduced by Rother et al. [26] with a generative model in a Markov Random Field (MRF) formulation that accounts for spatial coherence and appearance similarities between images. It is used for the detection of the same object in different scenarios: in front of different backgrounds and/or observed from different viewpoints. In the same direction, the work of [13] uses an MRF solved with the max-flow algorithm in a graph implementation, aiming at maximizing the similarity between a pair of images. MRF formulation of the co-segmentation problem is also proposed in [24] where the common foreground in a pair of images is quantified by histogram matching. It is worth noting that although these approaches model the problem with an MRF, the inference is solved in different ways. A different approach was proposed by Joulin et al. [14], who combine bottom-up unsupervised clustering with top-down supervised classification, maximizing spatial and appearance consistency within an image and the separability of two classes between different images. Extending co-segmentation to larger image collections, Russell et al. [27] build the solution from initial over-segmentation sets. Based on the bag-of-words model, they extract visual words, then topics, and the common foreground is built by choosing good segments within each topic. In [3], the common foreground in the image collection is extracted in an interactive manner, where the user decides what the target is, and a Generative Mixture Model-based framework is driven by active learning based on the user's manual labeling.

Co-segmentation was recently applied to the problem of

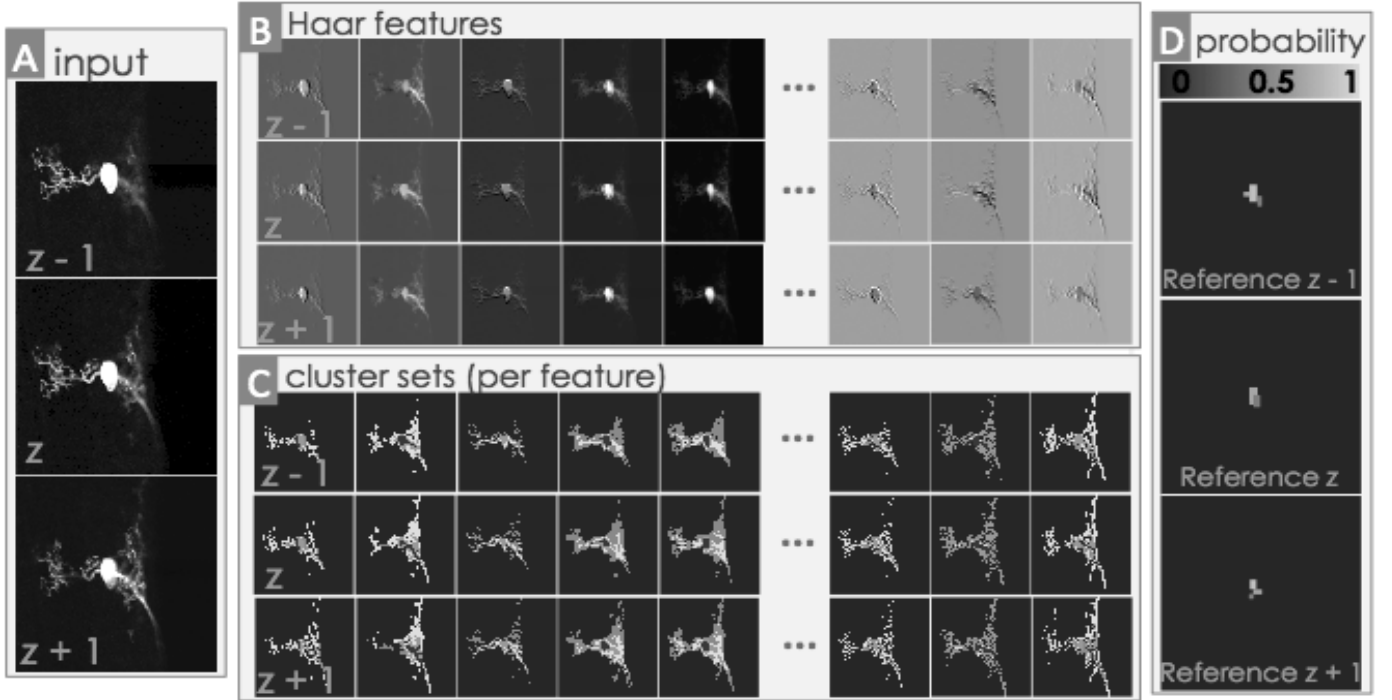


Fig. 5. Haar features, their clustering and estimation of the reference region. (A) Images from the input stack at successive depths. (B) Haar-based intensity features calculated for each image. (C) Clustering outcomes $C_h^{(z-1)}$, $C_h^{(z)}$ and $C_h^{(z+1)}$ for features $h = 1, \dots, H$. (D) Estimated reference probability maps $\mathcal{P}^{(z-1)}(\mathbf{x})$, $\mathcal{P}^{(z)}(\mathbf{x})$ and $\mathcal{P}^{(z+1)}(\mathbf{x})$, $\forall \mathbf{x} \in \Omega$, from eq. (6).

estimating 2D neuron boundaries from electron microscopy data [35], where the objective function to be minimized penalizes disagreements between the segmentation outcomes from two closely correlated images (successive images in the stack). However, the aim of this work was to segment boundaries ignoring the actual neuron morphology.

Here, we assume intensity continuity/smoothness along the z -axis (depth), i.e. that successive images are correlated. If a region of interest exists at a given depth, then part of it should also exist at neighboring depths. We use this as a soft constraint to account for progressively appearing/disappearing regions over depth, which depicts the arbitrary 3D topology of the neuron compartments. We also assume that the entire soma is present in the examined volume.

A. Initial segmentation

Similarly to e.g. [14], we first create superpixels from each image in the stack with over-segmentation. Due to the data inhomogeneities in the xy plane and along the z -axis, and to obtain more robust intensity information, we use Haar-like features [34] of fixed size in 3D as shown in Fig. 4. Such masks are essentially based on the idea of wavelet decomposition, some of which (the two-box masks) approximate the sigmoid Haar basis functions. They provide coarse modeling of appearance, are not used for rich representation of texture (i.e., contrary to steerable/Gabor filters), but they can be computed very efficiently using the idea of the integral image [34]. Detailed texture modeling is not our scope, due to the high variability of intensity (lack of salient textures).

Let $\mathcal{I}^{(z)}$ be an image in the the stack, at depth $z = 1, \dots, Z$, and H be the total number of Haar features, using $n \times n \times m$ masks and taking into account images at neighboring depths

$\mathcal{I}^{(z \pm \delta z)}$, $\delta z = 1, \dots, (m-1)/2$. In our experiments, and for $1024 \times 1024 \times 30$ dataset size, we set $\{n = 25, m = 5\}$ and $H = 20$ features.

We segment $\mathcal{I}^{(z)}$ using each feature $h = 1, \dots, H$ separately, and we obtain H segmentation outcomes $C_h^{(z)}$. Here, we adopt the k-means algorithm, although other methods can be used (e.g. normalized cuts as in [27], [14]). Panel A in Fig. 5 illustrates three successive images in the stack, panel B shows the calculated H features for each depth, while panel C shows the initial clustering $C_h^{(z)}$ of each feature. The goal is to combine the outcomes $C_h^{(\zeta)}$, $\zeta = z \pm \delta z$, to obtain the final result $\tilde{C}^{(z)}$ for $\mathcal{I}^{(z)}$.

Our co-segmentation approach is driven by shape, as we define it below, since this is what discriminates the individual compartments of our interest.

B. Shape representation

We integrate information about both the shape and the relative positions of the neuron compartments in the image domain. That is, we define a shape representation of a set of objects using distance functions.

Let $C_h^{(z)} = \{C_{h,k}^{(z)}\}_{k=1}^K$ be a segmentation outcome for feature h at depth z , where $C_{h,k}^{(z)}$ is the k -th segment and K is the total number of segments³. We consider a *reference segment* $C_s^{(z)}$, which is chosen as the region that best approximates a prior knowledge that we have for the data, and is calculated from all segmentation outcomes $\{C_h^{(z)}\}_{h=1}^H$, as we explain below.

³Note that k and K are independent from the unsupervised approach for creating initial regions, and therefore they are irrelevant from the cluster index and total number of clusters of the k-means algorithm that we use. Also, we consider fixed the total number of k-means clusters for the entire volume.

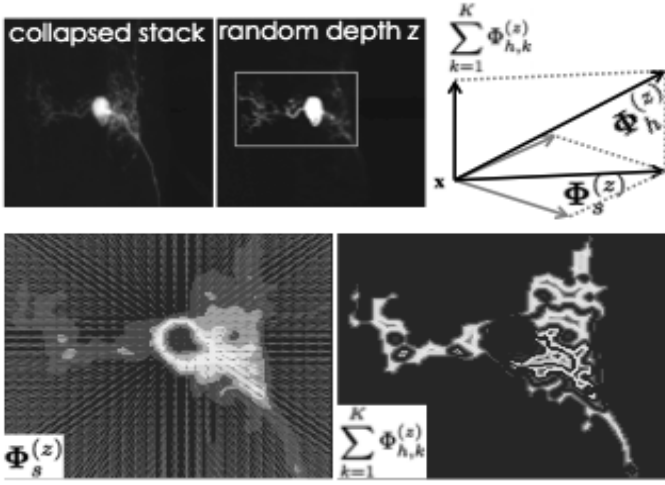


Fig. 6. Shape representation of a random over-segmentation outcome $C_h^{(z)}$. First row (from left to right): collapsed stack image; image at depth z with the box indicating the image part of our focus; general schematic representation of the shape as a vector field, at $\mathbf{x} \in \Omega$. Second row (from left to right): an over-segmentation set $C_h^{(z)}$ with the reference $C_s^{(z)}$ being the dark region in the center and its directed distance $\Phi_s^{(z)}$ superimposed; visualization of $\sum_{k=1}^K \Phi_{h,k}^{(z)}$ for the distance functions $\Phi_{h,k}^{(z)}$ of all k segments, normalized in $[0, 1]$.

If Ω is the (2D) image domain and $\mathbf{x} \in \Omega$ denotes location in Cartesian coordinates, the *directed* (vector) distance function $\Phi_s^{(z)}$ of the estimated reference segment s at depth z describes its shape but also the relative positions of all segments $\{C_{h,k}^{(z)}\}_{k=1}^K$,

$$\Phi_s^{(z)} = \mathbf{d}(\mathbf{x}, \mathcal{B}_s^{(z)}), \forall \mathbf{x} \in \Omega \quad (1)$$

where $\mathbf{d}(\mathbf{x}, \mathcal{B}_s^{(z)})$ is the vector distance of every $\mathbf{x} \in \Omega$ from the closest point on the reference segment boundary $\mathcal{B}_s^{(z)}$. The magnitude and direction of $\Phi_s^{(z)}$ represent the relative position of $\mathbf{x} \in \Omega$ and therefore of every segment (Fig. 6).

Moreover, the shape of each segment $C_{h,k}^{(z)}$ is described with the distance function,

$$\Phi_{h,k}^{(z)} = \begin{cases} d(\mathbf{x}, \mathcal{B}_{h,k}^{(z)}), & \forall \mathbf{x} \in C_{h,k}^{(z)} \\ 0, & \text{otherwise} \end{cases}, \quad (2)$$

where $d(\mathbf{x}, \mathcal{B}_{h,k}^{(z)})$ is the *undirected* distance of every $\mathbf{x} \in C_{h,k}^{(z)}$ from the closest point on the segment boundary $\mathcal{B}_{h,k}^{(z)}$ (Fig. 6).

Then, the topology (shapes and relative positions) at a single depth, given a segmentation outcome $C_h^{(z)}$, can be defined as a vector field,

$$\Phi_h^{(z)} = \left[\Phi_s^{(z)}, \sum_{k=1}^K \Phi_{h,k}^{(z)} \right], \quad (3)$$

given that $C_{h,i}^{(z)} \cap C_{h,j}^{(z)} = \emptyset$, $i \neq j$, i.e., for a given $\mathbf{x} \in \Omega$, $\Phi_{h,i}^{(z)}(\mathbf{x})$ and $\Phi_{h,j}^{(z)}(\mathbf{x})$ cannot both have non-zero values.

Estimation of the reference from soma segments. In our application, we consider a region of the soma, the least variable structure whose shape approximates a disk in the 2D domain, as the reference segment. If soma is over-segmented and/or there are regions from other compartments present at the given depth, then $C_s^{(z)}$ is chosen as the segment that best approximates our prior knowledge, i.e. best fits a disc.

Using the Bhattacharyya distance $D_h^{(z)}(k, disc)$ between the normalized shape histograms of $C_{h,k}^{(z)}$ and a disc, the

probability of the segment k being part of the reference can be formed as,

$$P(k = s | D_h^{(z)}(k, disc)) = 1 / \exp\{D_h^{(z)}(k, disc)\} \quad (4)$$

We define the auxiliary variable,

$$\lambda_{h,k}^{(z)}(\mathbf{x}) = \begin{cases} 1, & \forall \mathbf{x} \in C_{h,k}^{(z)} \\ 0, & \text{otherwise} \end{cases}, \quad (5)$$

which essentially is the Heaviside function of $\Phi_{h,k}^{(z)}$. Then, considering all segmentation outcomes $C_h^{(z)}$, $h = 1, \dots, H$, at depth z , we estimate the probability map $\forall \mathbf{x} \in \Omega$,

$$\mathcal{P}^{(z)}(\mathbf{x}) = \prod_{h=1}^H \left[\sum_{k=1}^K \lambda_{h,k}^{(z)}(\mathbf{x}) P(k = s | D_h^{(z)}(k, disc)) \right] \quad (6)$$

Note that K is not necessarily the same for all segmentation outcomes; however, in the above definition we consider a single K for notation simplicity. Fig. 5D shows $\mathcal{P}^{(z-1)}(\mathbf{x})$, $\mathcal{P}^{(z)}(\mathbf{x})$, $\mathcal{P}^{(z+1)}(\mathbf{x})$, $\forall \mathbf{x} \in \Omega$, where the reference segment is obtained by thresholding these maps.

C. Co-segmentation

Our objective is to combine the over-segmentation outcomes from all H features and m depths around z to obtain the final partitioning $\tilde{C}^{(z)}$, for every image in the stack. $\tilde{C}^{(z)}$ must contain segments of only three classes (soma, axon and dendrites), however the number of segments is unknown since more than one dendrites may exist.

Soma and axon have distinctive shapes as we describe above. We exploit this information to drive our task using the definitions in eqs. (1)-(3).

We formulate co-segmentation as a minimization of a cost function across all images in a given stack,

$$\begin{cases} \mathcal{E} = \sum_{z=1}^Z \varepsilon(z) \\ \varepsilon(z) = \varepsilon_z + \varepsilon_{\delta z} + \varepsilon_p \end{cases}, \quad (7)$$

where we introduce three kinds of loss terms that serve as constraints for appearance and shape, as described below.

(a) Local appearance homogeneity. We penalize inconsistencies among the sets $\{C_h^{(z)}\}_{h=1}^H$. Assume that two features h_1 and h_2 , $h_1 \neq h_2$, produce two segmentation outcomes $\{C_{h_1,k}^{(z)}\}_{k=1}^K$ and $\{C_{h_2,l}^{(z)}\}_{l=1}^L$, where K and L are the numbers of segments for each case. We want to detect which segments from one set match spatially the segments from the other, and penalize mismatches between spatially overlapping segments.

We define a *disagreement* term between two segments k and l produced from clustering two features h_1 and h_2 , as

$$\begin{aligned} \Delta_{h_1,h_2}^{(z)}(k,l) &= \\ &= \int_{\Omega} \delta_{h_1,h_2}^{(z)}(k,l) \left[C_{h_1,k}^{(z)} \cup C_{h_2,l}^{(z)} - C_{h_1,k}^{(z)} \cap C_{h_2,l}^{(z)} \right](\mathbf{x}) d\mathbf{x}, \end{aligned} \quad (8)$$

where

$$\delta_{h_1,h_2}^{(z)}(k,l) = \begin{cases} 1, & \text{if } C_{h_1,k}^{(z)} \cap C_{h_2,l}^{(z)} \neq \emptyset \\ 0, & \text{otherwise} \end{cases} \quad (9)$$

Then, the local segment homogeneity can be defined as,

$$\varepsilon_z = \sum_{\substack{(h_1, h_2) = 1 \\ h_1 \neq h_2}}^H \left[\sum_{k=1}^K \sum_{l=1}^L \Delta_{h_1,h_2}^{(z)}(k,l) \right] \quad (10)$$

(b) Local shape smoothness. If $\Phi_h^{(z)}$ is the shape of the

segmentation outcome $\mathcal{C}_h^{(z)}$ for feature h at depth z , we penalize shape variations that this feature yields over neighboring depths $z \pm \delta z$,

$$\epsilon_{\delta z} = \sum_{h=1}^H \left[\sum_{i=z-\delta z}^{z+\delta z} \sum_{\substack{j=z-\delta z \\ j \neq i}}^{z+\delta z} \frac{1}{|i-j|} |\Phi_h^{(i)} - \Phi_h^{(j)}| \right], \quad (11)$$

where $\frac{1}{|i-j|}$ gives higher weights to shape differences between images closer to each other with respect to depth.

Let us take into account the inherent properties of this implicit representation of shape (see also the vector illustration in Fig. 6), and consider the shape $\Phi = [\phi_x, \phi_y, \phi_z]$ of a segmentation set: the x and y elements correspond to the distance function of the reference and the z element corresponds to the distance representation of a segment if $\phi_z \neq 0$. Then (i) (ϕ_x, ϕ_y) are calculated using all H features and therefore can be considered constant with respect to the outermost summation in eq. (11), (ii) ϕ_x, ϕ_y and ϕ_z are pairwise orthogonal, and (iii) it has been shown that the distance-based shape representation satisfies the first-order continuity, i.e. $\frac{\partial \Phi}{\partial x}$, $\frac{\partial \Phi}{\partial y}$ and $\frac{\partial \Phi}{\partial z}$ are defined in the entire image domain. Therefore, eq. (11) can be decomposed into,

$$\epsilon_{\delta z}^r = \sum_{i=z-\delta z}^{z+\delta z} \sum_{\substack{j=z-\delta z \\ j \neq i}}^{z+\delta z} \frac{1}{|i-j|} |\Phi_s^{(i)} - \Phi_s^{(j)}|, \quad (12)$$

$$\epsilon_{\delta z}^s = \sum_{h=1}^H \left[\sum_{i=z-\delta z}^{z+\delta z} \sum_{\substack{j=z-\delta z \\ j \neq i}}^{z+\delta z} \frac{1}{|i-j|} |\Phi_{Kh}^{(i)} - \Phi_{Lh}^{(j)}| \right], \quad (13)$$

where $\Phi_{Kh}^{(i)} = \sum_{k=1}^K \Phi_{h,k}^{(i)}$ and $\Phi_{Lh}^{(j)} = \sum_{l=1}^L \Phi_{h,l}^{(j)}$ are the representations of the segmentation sets $\{\mathcal{C}_{h,k}^{(i)}\}_{k=1}^K$ and $\{\mathcal{C}_{h,l}^{(j)}\}_{l=1}^L$ for a given feature h at depths i and j respectively.

(c) Topological segment connectivity/separability. We are interested in partitioning a volume into three distinct compartment classes. This determines that merging segments from the initial clustering should successively reveal the desired shapes.

For the clustering outcome of each feature h , at depth z , we define a structure (hypermatrix) $\mathcal{M}_h^{(z)}$ with size $K \times K$, where K is the total number of estimated segments. Each element $\mathcal{M}_h^{(z)}(k_1, k_2)$ is the shape histogram of $\mathcal{C}_{h,k_1}^{(z)} \cup \mathcal{C}_{h,k_2}^{(z)}$. To avoid redundancies, $\mathcal{M}_h^{(z)}$ is a triangular matrix with the main diagonal consisting of the shape histograms of the individual segments. Moreover, taking into account the spatial coordination of the segments, we only allow for merging within neighborhoods, which makes $\mathcal{M}_h^{(z)}$ sparse.

Let q_d and q_e be the normalized shape histograms of an average soma (disc) and axon (elongated structure) estimated manually from existing datasets. Note that both compartments have conceptually distinct shapes and therefore it is possible to obtain their shape priors individually, although their relative topology is highly variable. Then the Bhattacharyya distances $D[\mathcal{M}_h^{(z)}(k_1, k_2), q_d]$ and $D[\mathcal{M}_h^{(z)}(k_1, k_2), q_e]$ indicate similarity with the desired shapes. Let

$$\alpha_h^{(z)}(k_1, k_2) = \min \{D[k_1 \cup k_2, k_1], D[k_1 \cup k_2, k_2]\}, \quad (14)$$

where

$$\begin{cases} D[k_1 \cup k_2, k_1] = D[\mathcal{M}_h^{(z)}(k_1, k_2), \mathcal{M}_h^{(z)}(k_1, k_1)] \\ D[k_1 \cup k_2, k_2] = D[\mathcal{M}_h^{(z)}(k_1, k_2), \mathcal{M}_h^{(z)}(k_2, k_2)] \end{cases},$$

penalize shape inconsistencies before and after merging segments k_1 and k_2 . Also, let

$$\beta_h^{(z)}(k_1, k_2) = \min \{D[\mathcal{M}_h^{(z)}(k_1, k_2), q_d], D[\mathcal{M}_h^{(z)}(k_1, k_2), q_e]\}, \quad (15)$$

which indicates the highest similarity between a merging outcome and the two shape priors. We define the cost term,

$$\epsilon_p = \sum_{h=1}^H \left[\sum_{k_1=1}^K \sum_{k_2 \geq k_1}^K \alpha_h^{(z)}(k_1, k_2) \beta_h^{(z)}(k_1, k_2) \right], \quad (16)$$

which penalizes large shape variations before and after merging (with α) and dissimilarities with the desired priors (with β), over all features.

D. Cost minimization

The minimization of the segmentation cost posed in (7), using the definitions in eqs. (10), (11)-(13), (16), is a combinatorial problem, where segments from different feature clustering outcomes over different depths are pairwise merged to successively produce larger segments. Various methods have been proposed in the recent co-segmentation literature describing global optimization solutions, e.g. as Markov Random Fields [26], [13]. The most straightforward, but also most computationally demanding, approach would be to solve the minimization as an $N \times M \times Z \times H$ MRF, for $N \times M \times Z$ image stacks, over H features. The construction of a graph according to [13] can also be adopted, considering the segments as superpixels (replacing the pixels in the graph). We describe the steps of a bottom-up solution, according to which the complexity reduces monotonically during segment merging.

Given an image stack $\{\mathcal{I}^{(z)}\}_{z=1}^Z$:

- (i) For every $\mathcal{I}^{(z)}$, calculate the initial segmentation outcomes $\mathcal{C}_h^{(z)}$, $h = 1, \dots, H$, consisting of $K_h^{(z)}$ number of segments.
- (ii) For every $\mathcal{I}^{(z)}$, estimate the reference segment $\mathcal{C}_s^{(z)}$ from eq. (6). Produce Z references.
- (iii) For every $\mathcal{I}^{(z)}$, calculate H shapes $\Phi_h^{(z)}$. Produce $H \times Z$ shape representations.
- (iv) Calculate the cost terms ϵ_z , $\epsilon_{\delta z}^r$, $\epsilon_{\delta z}^s$, ϵ_p , and the total cost \mathcal{E} .
- (v) Merge segments within the sets $\mathcal{C}_h^{(z)}$ for each h and z independently, in a pairwise manner, and keep the merged segments that yield the minimum total energy $\mathcal{E}' \leq \mathcal{E}$. Specifically, $\forall z \in [1, Z]$:

- calculate $\frac{H \times (H-1)}{2}$ disagreement matrices $\Delta_{h_1, h_2}^{(z)}$ from eq. (8), to account for all pairwise segmentation outcome disagreements for the H features.

- For every pair of features h_1 and h_2 , merge the segments that simultaneously yield lower values for $\Delta_{h_1, h_2}^{(z)}$ and

$$\sum_{h=\{h_1, h_2\}} \left[\sum_{i=z-\delta z}^{z+\delta z} \sum_{\substack{j=z-\delta z \\ j \neq i}}^{z+\delta z} \frac{1}{|i-j|} |\Phi_{Kh}^{(i)} - \Phi_{Lh}^{(j)}| \right]$$

This step builds homogeneous segments that satisfy appearance and shape smoothness, that is it produces monotonically decreasing appearance and shape disagreement between two feature segmentation outcomes at a given depth, by conditionally decreasing the number of segments.

- (vi) Solve the above joint minimization problem recursively, over all depths $z \in [1, Z]$, repeating steps (ii)-(v). In our implementation we used the graph-based Dijkstra's shortest path algorithm [5]. However, due to the limited number of examined images (Z) and neighbors over depth ($2\delta z$), the recursive solution is trivial using most known optimization approaches (e.g., dynamic programming).

Note that in the above procedure we only consider pairs of segments that are spatial neighbors in the image domain.

III. RESULTS

Our MARCM experiments and imaging studies have thus far yielded over 150 high-resolution image stacks of 28 unique larval MN subtypes. We analyzed 34 randomly chosen datasets depicting 4 MN subtypes (MN1,9,15,16). Manual identification of these MNs agrees with the results of previous studies that focused on dendritic patterns [16] and presynaptic (axonal) patterns of connectivity [12].

In all datasets, the estimated and manually labeled compartment subvolumes largely coincide, which is sufficient for the desired morphology-based MN recognition.

A. Accuracy

We validated the accuracy of our method pixel-wise, by defining as error the percentage (%) of misclassified pixels with respect to the compartment area (2D) and volume (3D),

$$error_{dim}^{comp} = \frac{|ground\ truth - estimated|}{ground\ truth} \quad (17)$$

Here we report [*average, worst-case*] errors from two comparison approaches:

- (i) We manually traced soma, axon and dendrites boundaries for each image in a given stack and compared the resulting areas with our results. In average, over all depths in a stack, the 2D segmentation errors were: $error_{2D}^{soma} = [2.3, 6.8]$, $error_{2D}^{axon} = [4.1, 5.7]$, and $error_{2D}^{dendr} = [11.3, 20.4]$.

- (ii) We interpolated the manually traced boundaries over depth, calculated the 3D volume, and compared it with our estimated volume. The [*average, worst-case*] segmentation errors in 3D were: $error_{3D}^{soma} = [5.1, 7.9]$, $error_{3D}^{axon} = [6.3, 7.2]$, and $error_{3D}^{dendr} = [10.8, 18.7]$.

As anticipated, the segmentation of the soma yields lower errors, due to the relatively homogeneous intensity, its smooth variation over depth, and the small shape variation. On the other hand, the intensity inhomogeneities and random shapes of the dendrites make their accurate segmentation more challenging. The higher errors we report for the estimation of the volumes are mainly due to the interpolation of the 2D ground truth boundaries.

Fig. 7 shows qualitative results of our approach. The left side of panel (A) shows an example of initialization for our

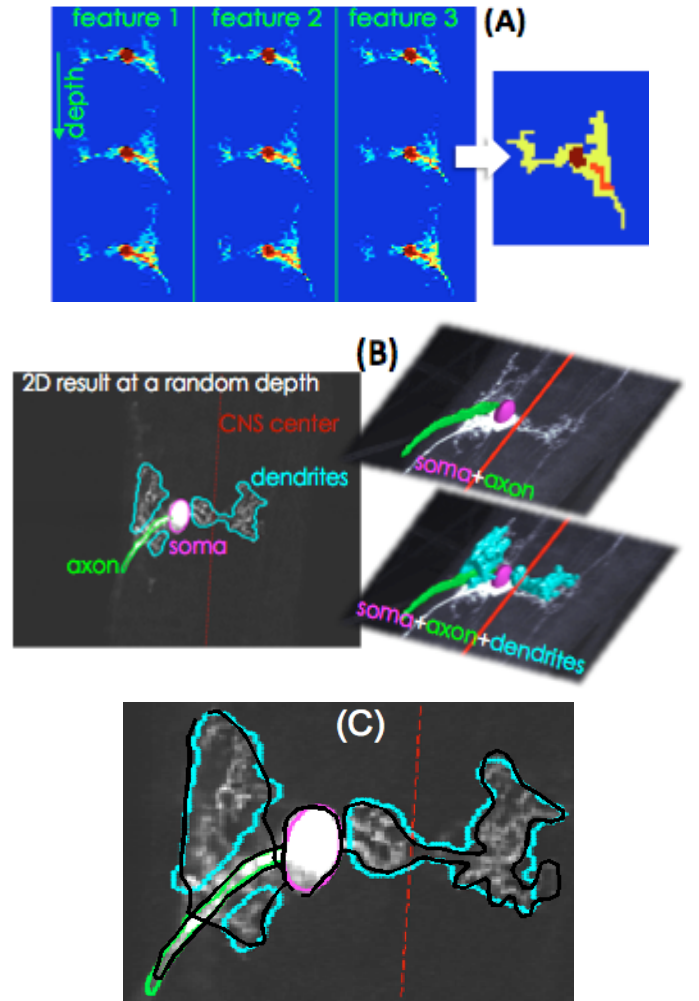


Fig. 7. (A) Co-clustering using three Haar features over three successive images in the stack. Left: individual over-clustered features. Right: co-segmentation result at a single depth. (B) Indicative segmentation result for a given dataset. Left: segmentation of a random image in the stack; the CNS center is also illustrated with a red line. Right: result in 3D. (C) Illustration of the solution at a random depth (same as in (B)), with respect to manual boundary tracing (ground-truth) shown with black lines.

method, over three successive depths in the stack, using three Haar features. Essentially, our approach splits and merges such spatial segments, taking into account neighboring images along depth. In this example, the right side of the panel shows the cross-section of the final result at the given depth. Panel (B) shows a result in 2D (cross-section at a random depth) and in 3D (see legend). Panel (C) illustrates a magnification of the result in 2D, with the black outlines showing the manual tracing of the compartments used as ground-truth in eq.(17).

The most relevant approach in the literature to compare our method with is the multi-compartment geometric deformable model (MGDM) [7], which must be initialized inside each distinct area/volume of interest. An obvious advantage of our method is that it does not require such initialization, and therefore the bottom-up compartment estimation is achieved without any *a priori* known topology. We tested the performance of MGDM for the 2D segmentation of the collapsed-stack neuron images and the segmentation of the neuron volume by extending the method into 3D.

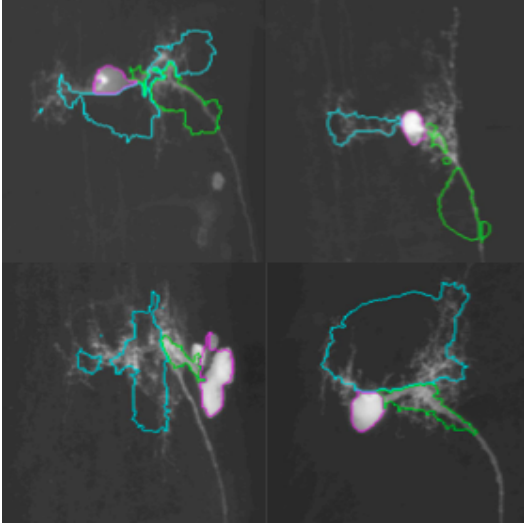


Fig. 8. Segmentation of the collapsed-stack images of four neurons, using the multi-compartment geometric model in [7].

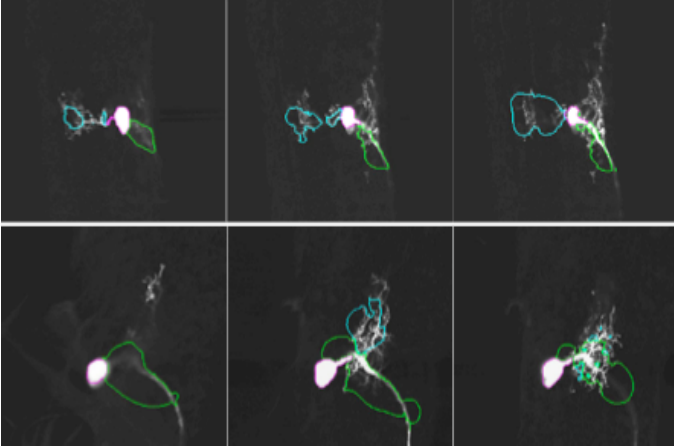


Fig. 9. Three-dimensional segmentation using a 3D extension of MGDM [7]: depth instances are shown for each neuron volume (row).

Fig. 8 illustrates the images of four motor neurons, with the 2D MGDM results superimposed: while somata are relatively accurately segmented, due to the smooth high intensity, axons and dendrites could not be captured. This is due to the intensity inhomogeneities and the lack of shape prior information. In all cases we initialized the method with a single line-seed inside each region of interest. We also observed that different initializations produce different segmentation results. Fig. 9 shows three depth instances (in each row) of the segmentation of two neuron volumes, using the 3D extension of MGDM.

We also tested the performance of more straightforward approaches, namely direct intensity clustering (fuzzy c-means and graph-cuts - see [11] for a review) and deformable models, such as our method in [31]. We first segmented the neuron volumes, and then partitioned the results into the distinct compartments manually, since part-based labeling is not an inherent process in such methods. The best and worst classification errors we obtained were: soma \Rightarrow [6.2, 9.4]; axon \Rightarrow [7.1, 9.8]; dendrites \Rightarrow [12.1, 19.1], where no single method performed better than the others for all datasets. Also, graphical model-based classification using conventional Markov and Conditional Random fields was not feasible, since no training can capture the high variability in the intensity,

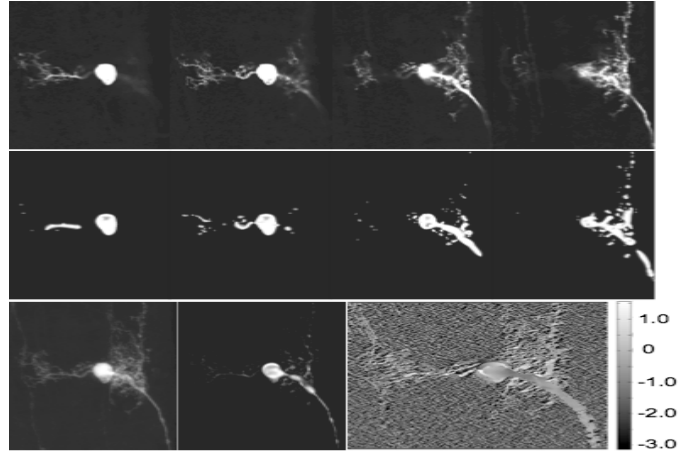


Fig. 10. Two- and three-dimensional Hessian-based Frangi filter [8], [2] for the estimation of the neuron compartments. First row: four images of the neuron stack; second row: the corresponding filter results; third row: the 2D filter applied to the collapsed-stack image (the estimated directionality is shown in the rightmost panel).

across datasets and within the same dataset (over depth).

Finally, we examined how the multi-scale Hessian-based filter of Frangi et. al [8], and its N-dimensional extension [2] can be used to extract the axon and soma subvolumes. As shown in Fig. 10, this type of filtering enhances the tubular-like structures of a neuron volume, however, its capability of partitioning the desired compartments is limited: (a) soma and axon cannot be segmented without additional global shape information, and (b) the dendrites cannot be accurately captured due to the lack of sufficient resolution (also see section I-C). The first row of Fig. 10 illustrates four images from a stack, while the second row shows the corresponding (3D) filter responses. In the third row, the 2D vesselness is estimated (middle) from the collapsed-stack image (left); the right panel illustrates the directionality of the detected vessel-like structures (notice the smoother directionality in the soma-axon region). From these images it becomes apparent that while such filter can be used to approximately locate soma and axon, it cannot be used for the actual partitioning of the desired compartments.

B. Solution stability

We validated the stability of our solution for different initializations, namely different initial over-segmentation sets for each feature and depth: $\{C_h^{(z)}\}_{h=1}^H$, $z = 1, \dots, Z$. The plots in Fig. 11A show the segmentation errors for the three compartments over 100 different initial over-segmentations with k-means. Fig. 12 illustrates the inconsistencies of k-means: the right image shows the normalized frequency with which pixels change clusters.

Fig. 11B shows the error in estimating the reference (soma region) at a given depth from eq. (6),

$$error^{ref} = \frac{\left| \mathcal{A}[\cap_{r=1}^{100} C_s^{(z)}(r)] - \mathcal{A}[C_s^{(z)}(i)] \right|}{\mathcal{A}[\cap_{r=1}^{100} C_s^{(z)}(r)]}, \quad (18)$$

where $\cap_{r=1}^{100} C_s^{(z)}(r)$ denotes the intersection of the estimated references over all initializations, $C_s^{(z)}(i)$ is the reference from the i -th initialization, and $\mathcal{A}[\cdot]$ denotes area.

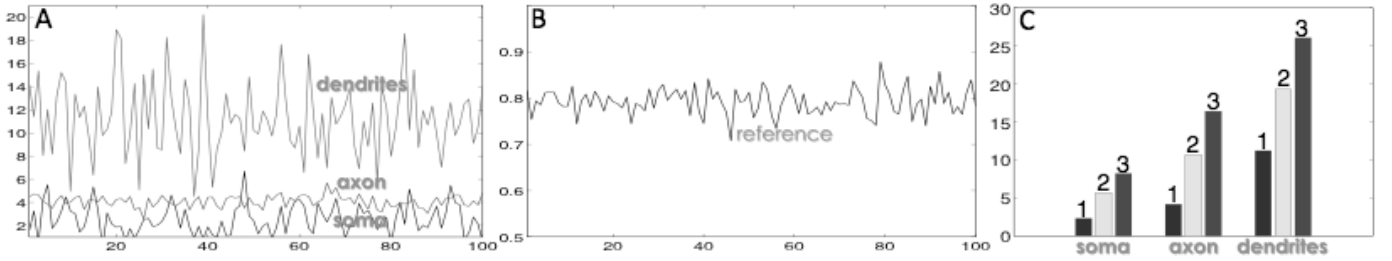


Fig. 11. Solution stability for different segment initializations. The x -axis in (A) and (B) corresponds to repetitions of the k-means algorithm (also see Fig. 12) that produce different segments as initialization for our method. (A) Average segmentation errors calculated from eq. (17) for each neuron compartment separately. (B) Variation in the reference segment estimation according to eq. (18). (C) Segmentation errors for each compartment, where each numbered bar corresponds to a different sampling factor that determines neighboring images along z : $1 = \{\mathcal{I}^{(z-2)}, \mathcal{I}^{(z-1)}, \mathcal{I}^{(z)}, \mathcal{I}^{(z+1)}, \mathcal{I}^{(z+2)}\}$, $2 = \{\mathcal{I}^{(z-4)}, \mathcal{I}^{(z-2)}, \mathcal{I}^{(z)}, \mathcal{I}^{(z+2)}, \mathcal{I}^{(z+4)}\}$, $3 = \{\mathcal{I}^{(z-6)}, \mathcal{I}^{(z-3)}, \mathcal{I}^{(z)}, \mathcal{I}^{(z+3)}, \mathcal{I}^{(z+6)}\}$.

We also validated the robustness of our method with respect to the correlation between successive images in the stack. For that purpose, we considered different sampling factors along z , i.e. images at different distances from each other. We recorded the segmentation errors from eq. (17) for each compartment separately, as shown in Fig. 11C. As anticipated, and similarly to existing co-segmentation methods, the more correlated the considered images, the higher the segmentation accuracy. In our framework, when neighboring images are far from each other along z , the intensity continuity (smoothness) assumption is violated.

Finally, Fig. 13 shows some indicative results of our method for neuron reconstruction and compartment-based labeling. For visualization purposes, the reconstructed somata and axons are illustrated as surfaces; the dendrites are represented with randomly sampled points from the obtained boundaries that were triangulated (for transparency).

IV. CONCLUSIONS AND DISCUSSION

The morphological properties of a neuron have a direct influence on patterns of synaptic connectivity. We developed an appearance and shape driven co-segmentation method for 3D reconstruction of the neuron morphology, in order to create 3D models standard for different motor neuron subtypes in the *Drosophila* nervous system. Such models will serve as a predictive tool for the assembly of motor circuits in the normal and mutant brain.

Beyond the specific application, the co-segmentation approach we described here balances the trade-off between shape and appearance in the segmentation of part-based structured objects: we bridge top-down (model fitting) methods, such as Active Shape Models (ASMs) [4] and bottom-up methods, such as the multi-compartment geometric models [7]. We described two key differences between our approach and these two families of methods: (a) the relative topology of the compartments is fixed but their shapes are highly varying; therefore ASMs cannot be applied due to the linearity of the employed Principal Component Analysis; (b) multi-compartment geometric models require labeled initializations within the different parts, i.e., consider prior knowledge for topology; on the contrary, in our approach topology is discovered in a bottom-up fashion. Finally, the difference between our approach and existing co-segmentation methods can be summarized in that we drive segmentation using shape, while existing algorithms use appearance.

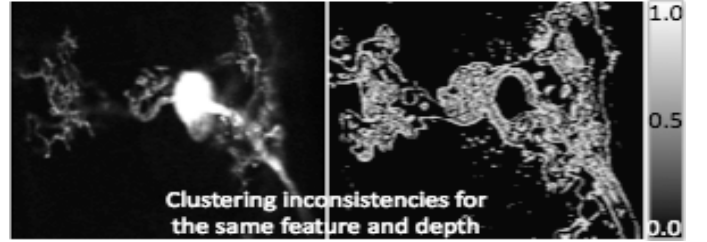


Fig. 12. Clustering inconsistencies for the same feature at the same depth (left: original image; right: result). Gray levels on the right panel illustrate in a normalized scale the *severity* of the k-means algorithm inconsistency, after 100 repetitions with the same number feature clusters and different centroid initializations. Brighter regions correspond to image pixels that change clusters frequently, while darker regions correspond to more stable pixels.

REFERENCES

- [1] Y. Al-Kofahi, N. Dowell-Mesfin, C. Pace, W. Shain, J.N. Turner, and B. Roysam, 'Improved Detection of Branching Points in Algorithms for Automated Neuron Tracing from 3D Confocal Images,' *Cytometry A*, 73(1): 36-43, 2008.
- [2] L. Antiga, 'Generalizing vesselness with respect to dimensionality and shape,' *The Insight Journal* (online), July 2007.
- [3] D. Batra, A. Kowdle, and D. Parikh, 'iCoseg: Interactive Cosegmentation with Intelligent Scribble Guidance,' in *Proc. IEEE Conf on Computer Vision and Pattern Recognition (CVPR)*, pp. 3169-3176, 2010.
- [4] T.F. Cootes, C.J. Taylor, D.H. Cooper, and J. Graham, Active shape models - their training and application, *Computer Vision and Image Understanding*, 61(1): 38-59, 1995.
- [5] T.H. Cormen, C.E. Leiserson, R.L. Rivest, and C. Stein, *Introduction to Algorithms*, MIT Press and McGraw-Hill, pp. 595601, 2001.
- [6] A. Dima, M. Scholz, and K. Obermayer, 'Automatic segmentation and skeletonization of neurons from confocal microscopy images based on the 3-D wavelet transform,' *IEEE Trans on Image Processing*, 11: 790-801, 2002.
- [7] X. Fan, P.-L. Bazin, and J.L. Prince, 'A multi-compartment segmentation framework with homeomorphic level sets,' in *Proc. IEEE Conf on Computer Vision and Pattern Recognition (CVPR)*, pp. 1-6, 2008.
- [8] A.F. Frangi, W.J. Niessen, K.L. Vincken, and M.A. Viergever, 'Multiscale vessel enhancement filtering,' in *Proc. Medical Image Computing and Computer Assisted Intervention (MICCAI)*, 130-137, 1998.
- [9] G. Gonzalez, E. Turetken, F. Fleuret, P. Fua, 'Delineating Trees in Noisy 2D Images and 3D Image-Stacks,' in *Proc. IEEE Conf on Computer Vision and Pattern Recognition (CVPR)*, pp. 2799-2806, 2010.
- [10] L. Grady, G. Funka-Lea, 'Multi-Label Image Segmentation for Medical Applications Based on Graph-Theoretic Electrical Potentials,' in *Proc. European Conf on Computer Vision (ECCV)*, pp. 230-245, 2004.

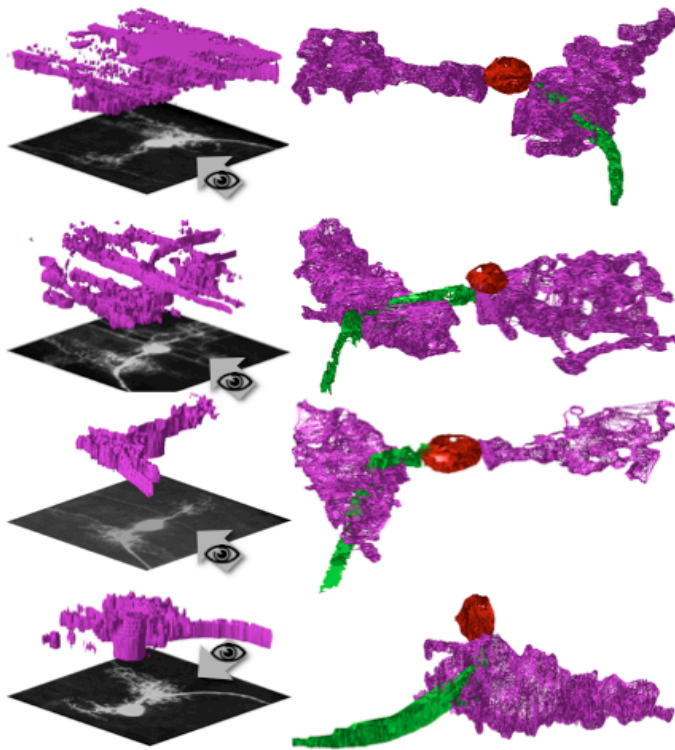


Fig. 13. Three-dimensional reconstruction of neuron morphology. Rows correspond to different datasets. Left column: collapsed-stack (mCD8-stained) single-neuron images obtained with MARCM, with the volumes illustrating the intensity in 3D. The arrows indicate the view angle in which the results are visualized. Right column: the 3D reconstruction results; the sub-volumes correspond to the neuron distinct compartments, namely soma (ellipsoid-like), axon (elongated) and dendrites (random shapes).

- [11] G. Guojun, C. Ma, and J. Wu, *Data Clustering: Theory, Algorithms and Applications*, ASA-SIAM Series on Statistics and Applied Probability, SIAM, Philadelphia, ASA, Alexandria, VA, 2007.
- [12] B. Hoang and A. Chiba, 'Single-cell analysis of Drosophila larval neuromuscular synapses,' *Dev Biol.*, 229: 55-70, 2001.
- [13] D.S. Hochbaum and V. Singh, 'An efficient algorithm for co-segmentation,' in *Proc. Int'l Conf. on Computer Vision (ICCV)*, pp. 269-276, 2009.
- [14] A. Joulin, F. Bach, and J. Ponce, 'Discriminative Clustering for Image Co-segmentation,' in *Proc. IEEE Conf on Computer Vision and Pattern Recognition (CVPR)*, pp. 1943-1950, 2010.
- [15] V. Kaynig, T. Fuchs, J.M. Buhmann, 'Neuron Geometry Extraction by Perceptual Grouping in ssTEM Images,' in *Proc. IEEE Conf on Computer Vision and Pattern Recognition (CVPR)*, pp. 2902-2909, 2010.
- [16] M.D. Kim, Y. Wen, and Y.N. Jan, 'Patterning and organization of motor neuron dendrites in the Drosophila larva,' *Dev Biol.*, 336: 213-221, 2009.
- [17] M. Landgraf, N. Sanchez-Soriano, G.M. Technau, J. Urban, and A. Prokop, 'Charting the Drosophila neuropile: a strategy for the standardised characterisation of genetically amenable neurites,' *Dev Biol.*, 260: 207-225, 2003.
- [18] M. Landgraf, T. Bossing, G.M. Technau, and M. Bate, 'The origin, location, and projections of the embryonic abdominal motoneurons of Drosophila,' *J. Neurosci.*, 17: 9642-9655, 1997.
- [19] L. Landmesser, 'The distribution of motoneurons supplying chick hind limb muscles,' *J. Physiol.*, 284: 371-389, 1978.
- [20] L. Landmesser, 'The development of motor projection patterns in the chick hind limb,' *J. Physiol.*, 284: 391-414, 1978.
- [21] T. Lee and L. Luo, 'Mosaic analysis with a repressible cell marker for studies of gene function in neuronal morphogenesis,' *Neuron*, 22: 451-461, 1999.
- [22] Q. Li, X. Zhou, Z. Deng, M. Baron, M.A. Teylan, Y.Kim, and S.T.C. Wong, 'A Novel Surface-based Geometric Approach for 3D Dendritic Spine Detection from Multi-photon Excitation Microscopy Images,' in *Proc. Int'l Symposium on Biomedical Imaging (ISBI)*, pp. 1255-1258, 2009.
- [23] Mahr and H. Aberle, 'The expression pattern of the Drosophila vesicular glutamate transporter: a marker protein for motoneurons and glutamatergic centers in the brain,' *Gene Expr Patterns*, 6: 299-309, 2006.
- [24] L. Mukherjee, V. Singh, and C.R. Dyer, 'Half-Integrality based Algorithms for Cosegmentation of Images,' in *Proc. IEEE Conf on Computer Vision and Pattern Recognition (CVPR)*, pp. 2028-2035, 2009.
- [25] H. Peng, Z. Ruan, D. Atasoy, S. Sternson, 'Automatic reconstruction of 3D neuron structures using a graph-augmented deformable model,' *Bioinformatics*, 26(12): 38-46, 2010.
- [26] C. Rother, V. Kolmogorov, T. Minka, and A. Blake, 'Co-segmentation of image pairs by histogram matching incorporating a global constraint into MRFs,' in *Proc. IEEE Conf on Computer Vision and Pattern Recognition (CVPR)*, 1: 993-1000, 2006.
- [27] B.C. Russell, W.T. Freeman, A.A. Efros, J. Sivic, and A. Zisserman, 'Using multiple segmentations to discover objects and their extent in image collections,' in *Proc. IEEE Conf on Computer Vision and Pattern Recognition (CVPR)*, 2: 1605-1614, 2006.
- [28] A. Schmid, A. Chiba, and C.Q. Doe, 'Clonal analysis of Drosophila embryonic neuroblasts: neural cell types, axon projections and muscle targets,' *Development*, 126: 4653-4689, 1999.
- [29] S. Schmitt, J.F. Evers, C. Duch, M. Scholz, and K. Obermayer, 'New Methods for the Computer-Assisted 3D Reconstruction of Neurons from Confocal Image Stacks,' *NeuroImage*, 23(4): 1283-1298, 2004.
- [30] A.M. Seggio, A. Narayanaswamy, B. Roysam, and D.M. Thompson, 'Self-aligned Schwann cell monolayers demonstrate an inherent ability to direct neurite outgrowth,' *J. Neural Eng.*, 7(4): 046001, 2010.
- [31] G. Tsechpenakis, J. Wang, B. Mayer, and D. Metaxas, 'Coupling CRFs and Deformable Models for 3D Medical Image Segmentation,' in *Proc. IEEE Mathematical Methods in Biomedical Image Analysis*, pp. 1- 8, 2007.
- [32] C. Uehara, C. Colbert, P. Saggau, and I.A. Kakadiaris, 'Towards automatic reconstruction of dendrite morphology from live neurons,' in *Proc. Int'l Conf of the IEEE EMBS*, pp. 1798-1801, 2004.
- [33] S. Urban, S.M. OMalley, B. Walsh, A. Santamaria-Pang, P. Saggau, C. Colbert, and I.A. Kakadiaris, 'Automatic Reconstruction of Dendrite Morphology from Optical Section Stacks,' in *Proc. Int'l Workshop on Computer Vision Approaches to Medical Image Analysis*, pp. 190-201, 2006.
- [34] P. Viola and M. Jones, 'Rapid object detection using boosted cascade of simple features,' in *Proc. IEEE Conf on Computer Vision and Pattern Recognition (CVPR)*, pp. 511-518, 2001.
- [35] S.N. Vitaladevuni, R. Basri, 'Co-Clustering of Image Segments Using Convex Optimization Applied to EM Neuronal Reconstruction,' in *Proc. IEEE Conf on Computer Vision and Pattern Recognition (CVPR)*, pp. 2203-2210, 2010.
- [36] E. Vrieseling and S. Arber, 'Target-induced transcriptional control of dendritic patterning and connectivity in motor neurons by the ETS gene Pea3,' *Cell*, 127: 1439-1452, 2006.
- [37] X. Yuan, J.T. Trachtenberg, S.M. Potter, and B. Roysam, 'MDL Constrained 3-D Grayscale Skeletonization Algorithm for Automated Extraction of Dendrites and Spines from Fluorescence Confocal Images,' *Neuroinformatics*, 7(4): 213232, 2009.
- [38] W. Zhou, H. Li, and X. Zhou, '3D Dendrite Reconstruction and Spine Identification,' in *Proc. Medical Image Computing and Computer Assisted Intervention (MICCAI)*, 2: 18-26, 2008.